Implementation of non-uniform mesh in non-equilibrium Green's function simulations of quantum cascade lasers

Grzegorz Hałdaś[1]

Abstract

The non-equilibrium Green's function formalism method is used to simulate electronic transport in a quantum cascade laser. Calculations are performed in a real-space basis defined by the grid points. Implementation of a non-uniform mesh greatly improves the effectiveness of the method, allowing for realistic mapping of the device structure while keeping the numerical load achievable for personal computers. The results of simulations obtained employing a non-uniform mesh are shown to fit the experimental data much better than those using constant grid sampling.

Keywords Non-equilibrium Green's function · Quantum cascade laser · Electronic transport · Real-space basis · Non-uniform grid · Non-uniform mesh · Non-uniform sampling

1 Introduction

The non-equilibrium Green's function (NEGF) formalism is a powerful semiconductor device simulation method, which allows for the simultaneous consideration of carrier scattering and quantum coherence. However, this method is highly demanding, both conceptually and computationally, so in order to model real devices, a few simplifications must be made. They must be introduced in order to keep the numerical load, in terms of both time and memory, at a size achievable by currently available computers. For example, existing approaches implementing NEGF to simulate quantum cascade lasers (QCLs) that involve the basis being cut to several quantum states per QCL period [1] do not fully resolve for in-plane momentum [1], and all limit the analysis to at most three device modules [2–5]. As QCLs are purely unipolar devices, they all use effective-mass Hamiltonians limited to at most two bands [6], so the effect of band mixing is also simplified. QCL NEGF simulators utilize either the eigenfunction-like basis [2] or the real-space basis [1]. The former uses several quantum states per QCL period and

thus benefits from a relatively low numerical load, making this approach numerically efficient. Because of this, many important results, both theoretical and application-oriented, have been obtained with this approach [7–11]. The major simplification of the approach is that in reality, the basis is field-dependent, which is not taken into account when obtaining a self-consistent Schrödinger–Poisson solution. Using a real-space basis does not have this limitation. However, obtaining results with quantitative accuracy requires a very dense grid, making for a huge numerical load with this approach. This is a concern for both mid-infrared (mid-IR) devices, whose structures utilize fine layers of sub-nanometer width, and THz devices, which have a high well-to-barrier width ratio. In both cases, non-uniform sampling of device potential in the real space can significantly limit the size of the discretized Hamiltonian and make the method numerically efficient. Non-uniform sampling of real space within NEGF implementation has already been reported [12]. This study concerns ballistic, scattering-free transport in a high-electron-mobility transistor (HEMT). Our paper aims to implement a non-uniform mesh to study scattering transport in QCLs. We provide the detailed formulation for current density and scattering energies for the case of non-uniform mesh discretization (Sect. 3), which can also be used in other device-oriented NEGF solvers. In Sect. 4, the results obtained for uniformly and non-uniformly sampled THz QCL devices are compared in order to demonstrate the

✉ Grzegorz Hałdaś
   ghaldas@prz.edu.pl

[1] Department of Electronics Fundamentals, Faculty of Electrical and Computer Engineering, Rzeszow University of Technology, al. Powstańców Warszawy 12, 35-959 Rzeszow, Poland

benefits one can gain when using smart non-uniform sampling of the device potential in real space.

2 Device and model

The THz QCL selected for the simulations was described in [13]. This laser emits radiation at 2.4 THz frequency and uses an indirect phonon-photon pump scheme to achieve the population inversion [14]. Each module of the cascade consists of four wells and four barriers, with the widths tuned to tenths-of-nanometer precision. The design utilizes a GaAs/AlGaAs material system and contains layers with widths of **4.4**/6.45/**1.62**/7.15/**2.79**/10.455/**0.6**/4.965 nm, where the bold font indicates the barriers. The first well is delta-doped with Si to $n_s = 3.45 \times 10^{10}$ cm^{-2} near its center. The cascade in the THz QCL counts several hundred identical modules (260 for our device). Typically, to make the simulations feasible, 1–3 modules are considered, and the remainder are mimicked by appropriate boundary conditions. It is reasonable to assume that any position/energy-dependent quantity q remains unchanged after simultaneous space-energy shift, i.e., $q(z + L, E, k) = q(z, E - eFL, k)$, where L is the size of the single module and F is the average electric field due to the external bias. Such an assumption allows one to reduce the size of the structure, subjected to the calculations, to approximately one QCL module.

Precise mapping of the QCL layers in the growth direction requires the use of a grid with mesh size Δz of no more than the material's monolayer spacing. In the case of a uniform grid with $\Delta z = 0.2$ nm, one THz QCL module consists of $N = 193$ sites. The inclusion of several additional wells/barriers, which are necessary for the application of periodic boundary conditions, increases the number of sites to $N = 256$, which makes it nearly impossible to obtain the solution in the self-consistent Born approximation and in acceptable time. At the same time, even for dense mapping, accurate thickness of the layers is not preserved. For instance, for $\Delta z = 0.2$ nm, the layer mapping

error is approximately 1%. For $\Delta z = 0.6$ nm, the deviations from original layer widths can be as much as 10%. As discussed in the Introduction, a way to avoid these limitations is to keep the calculations in the real space and reduce the basis by non-uniform sampling. Our non-uniform sampling strategy is as follows: First, exact positions z_{int} of the interfaces are found, and sites are located symmetrically to the left/right of z_{int} in half-monolayer distance. The remaining space in each layer is then uniformly sampled, with spacing not exceeding some arbitrarily assumed maximum mesh size Δz_{max}. This strategy allows one to save many sites per QCL module, keeping the widths of subsequent layers (and thus the size of the whole device) unchanged. In Table 1, the number of sites for different values of the parameters Δz_{max} (non-uniform sampling) or Δz (uniform sampling) and the deviations of the QCL's intersubband transition energies from their reference values (calculated for a very dense uniform grid $\Delta z = 0.005$ nm) are gathered and compared. For the energy $E_{32} = E_3 - E_2$, which
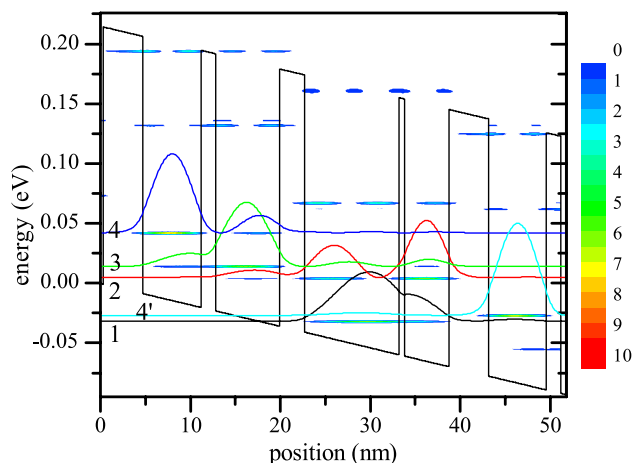

Fig. 1 Density of states (DOS) at $k = 0$ [color maps (eVnm)$^{-1}$] for a bias of 69 mV per period ($F = 17.96$ kV/cm). Lines show conduction band edge and DOS (for $k = 0$) at the energies where the local maximum is obtained (corresponding to major states in the QCL structure)

Table 1 Energy level shifts from reference values (column 2) resulting from the change in discretization grid method for non-uniform and uniform grid cases (see Fig. 1 for level enumeration)

	Uniform grid Δz (nm)			Non-uniform grid Δz_{max} (nm)		
	0.005	0.2	0.6	0.2	1	2
	r.e.	Change from reference energy (r.e.) (meV)				
E_{21}	36.570	−0.216	1.582	−0.035	0.103	0.311
E_{32}	9.348	−0.174	−1.758	0.006	0.091	0.412
E_{43}	28.197	0.696	−1.878	−0.011	0.011	0.270
E_{42}	37.545	0.522	−3.636	−0.005	0.102	0.683
E_{31}	45.918	−0.390	−0.176	−0.028	0.194	0.733
N	7684	193	65	196	53	36

Simulations were carried out for the model without scatterings for a bias of 69 mV per period ($F = 17.96$ kV/cm)

describes optical transition, the difference in the deviations for different grid size and sampling strategies can be huge: for example, for $\Delta z_{max} = 1$ nm (non-uniform sampling), the change is almost 20 times smaller than for $\Delta z = 0.6$ nm (uniform sampling). If we further increase Δz_{max} to 2 nm, the change is still four times smaller than for the $\Delta z = 0.6$ nm case. At the same time, the basis is almost twice as small as for uniform sampling. This improvement is achieved despite the fact that for the non-uniform finite difference scheme, the truncation error is only first order in Δz_{max} ($\mathcal{O}(\Delta z_{max})$) as compared with second-order accuracy characteristic of a homogeneous grid. One must remember, however, that the increase in Δz_{max} cannot go to arbitrary large values: It is well known that a one-dimensional (1D) discrete lattice has a cosine dispersion relation $E = 2t(1 - \cos(ka))$, where $t \equiv \frac{\hbar^2}{2m^*a^2}$, a is the lattice constant, and m^* is the effective mass. When a increases, the difference between the discretized (cosine) and continuous (parabolic) dispersions becomes large even for low energies. For this reason, a should be kept at a value that maintains the analysis close to the band edge. Numerically, it is equivalent to the condition $E_{max} << 4t$, where E_{max} is the maximum energy involved in the simulations. For example, for a GaAs conductor ($m^* = 0.067m_0$) and for $a = 2$ nm, the energy cosine bandwidth is $4t \cong 0.57$ eV. As can be seen in Fig. 2, a reasonable approximation can be obtained for energies lower than $E_{max} \cong 0.2$ eV $\approx 1.5t$. This limitation has been retained for the maximum grid size, i.e., $\Delta z_{max} \leq \sqrt{0.75\hbar^2/m^*E_{max}} \approx 0.2\lambda_{min}$, where λ_{min} is the particle minimum wavelength.
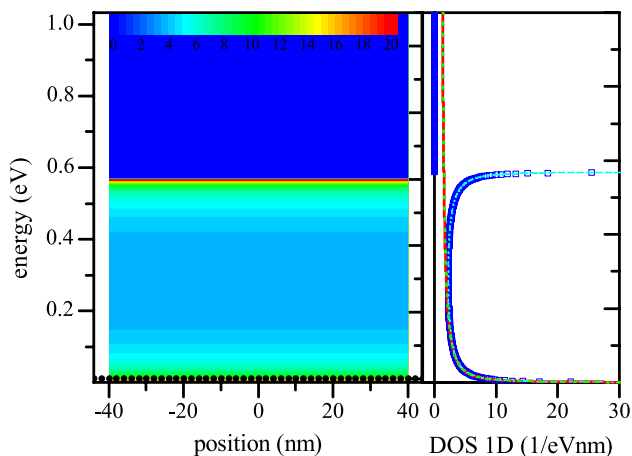
Fig. 2 (left) One-dimensional density of states (DOS) calculated within the NEGF formalism for a GaAs conductor $|z| \leq 40$ nm connected to semi-infinite leads $|z| > 40$ nm (color map). In the leads and device, uniform sampling with $\Delta z = 2$ nm is used. (right) DOS calculated at $z = 0$ (squares) compared with theoretical lines: (dashed) cosine dispersion $2/(\pi ta\sqrt{1 - (1 - E/2t)^2})$, (dotted) parabolic dispersion $(2/\pi\hbar)\sqrt{2m^*/E}$, (solid) calculated from an 8-band k·p model

3 Theory

So far, all QCLs are purely unipolar n-type devices, so the model uses a single-band effective-mass Hamiltonian, which accounts for mixing with the valence bands through energy-dependent effective mass $m(E, z) = m^*(z)\{1 + [E - E_c(z)]/E_g(z)\}$, where E is the total energy, $E_c(z)$ and $E_g(z)$ are the conduction band edge and band gap profiles, and z is the growth direction. The in-plane dynamics are included by kinetic energy terms with the same energy-dependent effective mass. Such a choice, which is not ultimate, preserves the in-plane non-parabolicity, comparable to the results predicted by the 8-band k·p method [15]. The full non-interacting Hamiltonian is expressed as

$$H = \frac{-\hbar^2}{2}\frac{d}{dz}\frac{1}{m(E, z)}\frac{d}{dz} + V(z) + \frac{\hbar^2 k^2}{m(E, z)}, \tag{1}$$

where the potential energy term $V(z) = E_c(z) + V_{sc}(z)$ comprises the conduction band edge profile $E_c(z)$ and the electron mean field term $V_{sc}(z)$, calculated self-consistently by the solution of the Poisson equation. As already mentioned, the calculations are made in real space, so the Hamiltonian of Eq. (1) is discretized and the grid points (non-uniformly spaced on the z-axis) define its base vectors; the discretized Hamiltonian **H** can then be evaluated in the matrix form following [16]

$$\mathbf{H}_{i,i} = V(z_i) + \frac{\hbar^2 k^2}{m(E, z_i)} - \mathbf{H}_{i,i+1} - \mathbf{H}_{i,i-1},$$
$$\mathbf{H}_{i,i\pm1} = -\frac{\hbar^2}{m(E, z_{i\pm})z_{i,i\pm1}(z_{i+1} - z_{i-1})}, \tag{2}$$

where discretization site i has coordinate z_i, sites i, j are at the distance $|z_j - z_i| \equiv z_{i,j}$, $z_{i\pm} = (z_{i\pm1} + z_i)/2$ are halfway between z_i and z_{i+1} or z_{i-1} and z_i, and $m(E, z_{i\pm}) \equiv \frac{1}{2}(m(E, z_{i+1}) + m(E, z_i))$. It stems from Eq. (2) that matrix **H** is non-Hermitian. The Dyson and Keldysh equations take the forms [17]

$$(E\mathbf{I} - \mathbf{H} - \mathbf{\Sigma^R})\mathbf{G^R} = \lambda, \tag{3}$$

$$(E\mathbf{I} - \mathbf{H} - \mathbf{\Sigma^R})\mathbf{G^<} = \mathbf{\Sigma^<}\mathbf{G^A}, \mathbf{G^A} = (\mathbf{G^R})^\dagger, \tag{4}$$

where **I** is the unity matrix, and **Σ**s and **G**s are the self-energy and Green's function matrices with the elements (i, j) linking the discretization sites at z_i and z_j. The matrix λ in Eq. (3) is a diagonal matrix with the elements $\lambda_{i,i} \equiv 2/(z_{i+1} - z_{i-1})$. For the Hamiltonian of Eq. (1), all **G**s are the functions of two parameters, i.e., total energy E and in-plane momentum modulus k: $\mathbf{G} = \mathbf{G}(E, k)$. The scattering self-energies that enter the formalism must be calculated with care. The usual formulation uses the Dyson equation in the form $(E\mathbf{I} - \mathbf{H} - \mathbf{\Sigma^R})\mathbf{G^R} = \mathbf{I}$, and so the Green's functions

have the units of energy^{-1}. In our case, the Green's functions are per energy×length. The necessary integration over space must not be omitted, in order to preserve the consistency. For instance, for the quasi-elastic approximation of scattering with acoustic phonons, the formulation for the self-energy in [18] is expressed as

$$\Sigma_{i,j}^{\mathbf{R},<} = \delta_{i,j} \frac{k_B T D^2}{4\pi^4 \rho v_s^2 a} \int dk^2 \mathbf{G}_{i,j}^{\mathbf{R},<},$$

where k_B is the Boltzmann constant, v_s, ρ, D are the sound velocity, the density, and the deformation potential in the host material, and a is the grid size. In our formulation, the integration over the spatial coordinate cancels term a, so that the correct formula for this self-energy is

$$\Sigma_{i,j}^{\mathbf{R},<} = \delta_{i,j} \frac{k_B T D^2}{4\pi^4 \rho v_s^2} \int dk^2 \mathbf{G}_{i,j}^{\mathbf{R},<}, \tag{5}$$

where $\mathbf{G}^{\mathbf{R},<}$ are calculated from Eqs. (3) and (4). A similar, straightforward transformation can be applied to other self-energies with diagonal-only entries, such as alloy disorder or interface roughness. For the interactions, which give non-local self-energies, i.e., ionized impurities and polar optical phonons, the transformations are less intuitive. Self-energies for polar optical phonons should be calculated as [18]

$$\Sigma_{i,j}^{\mathbf{R}}(E,k) = \frac{\beta}{\pi} \int \frac{d^2 q}{4\pi^2} I_{lo}(|z_i - z_j|, k, q)/\lambda_{j,j}$$
$$\times \left[n_B \mathbf{G}_{i,j}^{\mathbf{R}}(E + \hbar\omega, q) + (n_B + 1)\mathbf{G}_{i,j}^{\mathbf{R}}(E - \hbar\omega, q) \right.$$
$$\left. + \frac{1}{2}\left(\mathbf{G}_{i,j}^{<}(E - \hbar\omega, q) - \mathbf{G}_{i,j}^{<}(E + \hbar\omega, q)\right) \right], \tag{6}$$

and

$$\Sigma_{i,j}^{<}(E,k) = \frac{\beta}{\pi} \int \frac{d^2 q}{4\pi^2} I_{lo}(|z_i - z_j|, k, q)/\lambda_{j,j}$$
$$\times \left[n_B \mathbf{G}_{i,j}^{<}(E + \hbar\omega, q) + (n_B + 1)\mathbf{G}_{i,j}^{<}(E - \hbar\omega, q) \right], \tag{7}$$

where n_B is the Bose–Einstein factor for energy $\hbar\omega$, $\beta = e^2 \hbar\omega(\epsilon_\infty^{-1} - \epsilon_0^{-1})/2$, and I_{lo} is the integral calculated as

$$I_{lo}(|z - z'|, k, q)$$
$$= \int_0^{\pi/a} dq_z \frac{\cos(q_z(z - z'))}{\sqrt{(q_z^2 + q^2 + k^2 + q_0^2)^2 - 4k^2 q^2}}$$
$$\times \left(1 - \frac{q_0^2(q_z^2 + k^2 + q^2 + q_0^2)}{(q_z^2 + q^2 + k^2 + q_0^2)^2 - 4k^2 q^2} \right), \tag{8}$$

For the impurity scattering, the self-energies are [4]

$$\Sigma_{i,j}^{\mathbf{R},<}(E,k) = \frac{e^4}{16\pi^2 \epsilon^2} \int q dq I_{\mathrm{imp}}(z_i, z_j, k, q)/\lambda_{j,j}$$
$$\times \mathbf{G}_{i,j}^{\mathbf{R},<}(E, q),$$
$$I_{\mathrm{imp}}(z_i, z_j, k, q) = \sum_k \frac{1}{\lambda_{k,k}} N_D(z_k) \tag{9}$$
$$\times \int_0^{2\pi} d\theta \frac{e^{-\sqrt{q_0^2 + k^2 + q^2 - 2kq\cos\theta}(|z_i - z_k| + |z_j - z_k|)}}{q_0^2 + k^2 + q^2 - 2kq\cos\theta},$$

where $N_D(z)$ is the ionized impurity concentration profile, θ is the angle between vectors k and q, q_0 is the inverse Debye screening length, and ϵ is the static dielectric constant. In the case of non-uniform sampling, the calculation of integrals I_{lo} and I_{imp} is associated with a huge increase in computational effort and use of computer memory. However, as these integrals do not change when equations are iterated, they can be executed only once, tabulated and stored in computer memory. This is one more advantage of the chosen basis.

With the NEGF method, boundary conditions are applied through the contact self-energies. In our approach, the contact self-energy matrix $\Sigma_{\mathbf{C}}^{\mathbf{R}}$ has only two nonzero elements, namely, for the device's left boundary

$$\Sigma_{\mathbf{C}\ 1,1}^{\mathbf{R}} = \tau_{\mathrm{LD}} \mathbf{g}_{0,0}^{\mathbf{R}} \tau_{\mathrm{DL}}, \tag{10}$$

where $\mathbf{g}^{\mathbf{R}}$ is the Green's function of the (uncoupled) lead [19], and τ_{LD}, τ_{DL} are coupling elements. The method for calculating the function $\mathbf{g}^{\mathbf{R}}$, which imitates the boundary conditions appropriate for cascade structures, was described in [5, 20]. With a non-uniform grid, the coupling elements are calculated according to Eq. (2), i.e.,

$$\tau_{\mathrm{LD}} = \mathbf{H}_{0,1} = \frac{\hbar^2}{2} \frac{2}{(a_L + a_0)a_0} \frac{2}{m_L + m_1},$$
$$\tau_{\mathrm{DL}} = \mathbf{H}_{1,0} = \frac{\hbar^2}{2} \frac{2}{(a_0 + z_{1,2})a_0} \frac{2}{m_L + m_1}, \tag{11}$$

where $a_L \equiv |z_0 - z_{-1}|$, $a_0 \equiv |z_1 - z_0|$ (z_0, z_{-1} are the coordinates of the first and second site in the lead adjacent to the device), and $m_L = m(z_0)$, $m_1 = m(z_1)$. The right contact self-energy $\Sigma_{\mathbf{C}\ N,N}^{\mathbf{R}}$ can be similarly calculated.

With the diagonal elements of the Green's functions matrices, the spatial momentum-resolved densities of states (DOS) and densities of electrons (DOE) can be calculated as [19]

$$N_i(E,k) = -\frac{1}{\pi} \mathrm{Im}(\mathbf{G}_{i,i}^{\mathbf{R}}(E,k)),$$
$$n_i(E,k) = -\frac{1}{2\pi} \mathrm{Im}(\mathbf{G}_{i,i}^{<}(E,k)). \tag{12}$$

The integration over $\mathbf{k}$ gives z-resolved DOS and DOE. The formulation for current density requires reformulation with respect to [17]. The particle current flowing between internal site i and $i + 1$ (for some $E, \mathbf{k}$) [9] is expressed as

$$J_i = \frac{1}{\hbar A} \left[\mathbf{G}^<_{i,i+1} \mathbf{H}_{i,i+1} / \lambda_{i,i} - \mathbf{G}^<_{i+1,i} \mathbf{H}_{i+1,i+1} / \lambda_{i+1,i+1} \right], \quad (13)$$

where A is the cross-sectional area.

Optical gain can be calculated with the perturbation method of [7], adopted for the case of energy-dependent effective mass [21]. In that approach, the absorption coefficient is obtained from the real part of the complex conductivity, i.e., $\alpha \cong \Re(\sigma(\omega))/c\epsilon_0\sqrt{\epsilon_r}$ (the symbols have the usual meanings). The complex conductivity is obtained as $\sigma(\omega) = \delta J(\omega)/\mathcal{F}(\omega)$, where δJ is the current perturbation and $\mathcal{F}$ is the external radiation field. The current perturbation is calculated as

$$\delta J(\omega) = \frac{e}{\hbar A} \int \frac{dE}{2\pi} \mathrm{Tr}\{(\delta\mathbf{U}(\omega)\mathbf{Z} - \mathbf{Z}\delta\mathbf{U}(\omega))\lambda^{-1}\mathbf{G}^<(E) \\ + \mathbf{W}\delta\mathbf{G}^<(\omega, E)\}, \quad (14)$$

where $\delta\mathbf{U}$ is the perturbing potential, which can be calculated in the Coulomb gauge as $\delta\mathbf{U} = -e\mathcal{F}(\omega)\mathbf{W}/\hbar\omega$, $\mathbf{W} \equiv \lambda^{-1}(\mathbf{HZ} - \mathbf{ZH})$, and $\mathbf{Z}$ is the diagonal matrix ($\mathbf{Z}_{i,i} = z_i$). The perturbed lesser Green's function $\delta\mathbf{G}^<$ in the first approximation is given by [7]

$$\delta\mathbf{G}^<(\omega, E) = \mathbf{G}^\mathbf{R}(E + \hbar\omega)\delta\mathbf{U}(\omega)\mathbf{G}^<(E) \\ + \mathbf{G}^<(E + \hbar\omega)\delta\mathbf{U}(\omega)\mathbf{G}^\mathbf{A}(E). \quad (15)$$

4 Results

In order to illustrate the advantages of the method that uses non-uniform mesh, calculations for the THz QCL were carried out using uniform and non-uniform mesh. In the case of uniform sampling, $\Delta z = 0.6$ nm was assumed, which gave 87 sites of the simulation model. For non-uniform sampling, several values of $\Delta z_{max} = 0.8, 1, 1.2$ nm were tried. In Table 2, the current density and the maximum gain peak,

Table 2 The current density and maximum gain peak for different non-uniform grids calculated for the value of the field $F = 19.8$ kV/cm

Δz_{max} (nm)	Current density (kA/cm^2)	Max gain (1/cm)
1.2	1.25	59.5
1.0	1.23	57.7
0.8	1.22	57.0

calculated for the field $F = 19.8$ kV/cm, and different values of the parameters Δz_{max} are gathered and compared. As can be seen, the result "saturates" for $\Delta z_{max} \geq 1$ nm, so the latter was used in the following simulations. For $\Delta z_{max} = 1$ nm, the model counts 74 sites. For the discretization in E and k^2 spaces, the uniform grids were assumed with spacings of $dE = dE_k = \hbar^2 dk^2/2m^* = 1$ meV.

There were also included scattering self-energies for the interactions with (1) acoustic phonons in energy-averaged approximation [4], (2) screened, dispersionless optical phonons in the full non-local approximation (all off-diagonal elements of self-energy included) [18], (3) alloy disorder, (4) interface roughness with a Gaussian correlation function with correlation length $\Lambda = 9$ nm and asperity height $\Delta = 0.19$ nm [4], and (5) ionized impurities [4]. Calculations were performed for the temperature $T = 50$ K. The NEGF-Poisson solver [5] was used to obtain the self-consistent solution of the Dyson, Keldysh and Poisson equations. The boundary conditions for the Poisson equation ensured charge neutrality of the single module.

The results of the simulations are presented in Figs. 3 and 4. In Fig. 3, the current-voltage characteristics for uniform and non-uniform grid sampling are shown and compared with the experiment [13]. One can see that the characteristics for non-uniform grid sampling are much closer to the experimental data than those for a uniform grid.

A comparison of the simulated gain for non-uniform and uniform grid cases is shown in Fig. 4. In both cases, the gain was calculated for the value of the field in which the gain peak reached its maximum value, i.e., 19.8 and 19.2 kV/cm for non-uniform and uniform sampling, respectively. For the non-uniform grid case, the gain peak appears at 2.67 THz ($h\nu = 11$ meV) and reaches a value of ≈ 60 cm^{-1}, which slightly exceeds all optical losses [13]. This frequency is
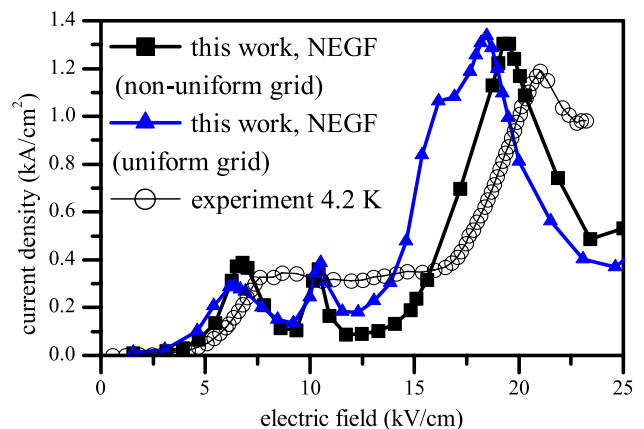
Fig. 3 Calculated I-V characteristics (filled symbols, i.e., squares for a non-uniform grid case, triangles for a uniform grid case) compared to the experiment (empty symbols) [13]
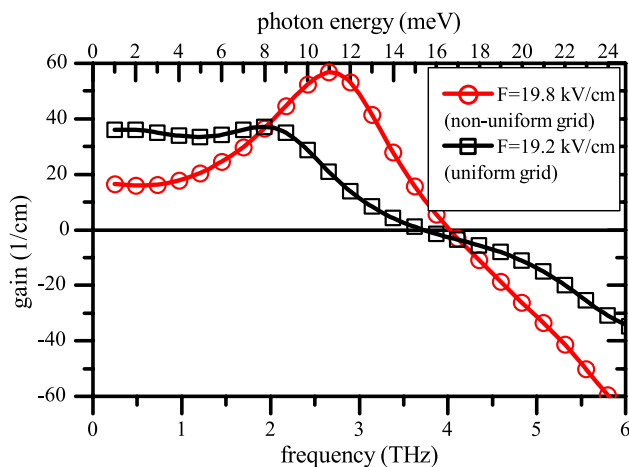
Fig. 4 Optical gain spectrum with maximum gain peak for uniform (square) and non-uniform (circle) grid cases

quite close to the experimental lasing frequency value of 2.4 THz. In the case of a uniform grid, a distinct peak of the gain cannot be observed. In this case, a broad gain peak (≈ 40 cm^{-1}) appears at 1.93 THz ($h\nu = 8$ meV), which is significantly lower than the experimental laser frequency. Moreover, the gain does not reach losses, so lasing is not predicted with this model.

The theoretical multi-valley I-V characteristic calculated with our implementation of the NEGF method is not observed in the experiment, which qualitatively reproduces the simulated behavior only for the lowest and the highest fields. For the medium-value fields, a plateau rather than oscillatory behavior is observed. This discrepancy is most probably caused by the evolving electric field domains [22]. In structures like the THz QCL, such domains are very likely to form due to the incomplete relaxation of carrier energy within one module [4]. Another difference between the simulated and experimental I-V curves is the shift of calculated resonance peaks to lower voltages. This shift can be attributed at least in part to the voltage drop observed at the Schottky-like junction between the top metal and top n$^+$ GaAs contact layer [22]. With respect to other simulation methods, it is worth mentioning that our I-V characteristic is in excellent agreement with the NEGF simulation performed with a Wannier state basis [13]. Better agreement between simulated and experimental I-V curves was achieved with the rate equation (RE) model combined with the density matrix (DM) method [13]. However, the gain peak achieved at 2.9 THz with the RE/DM method agrees substantially less with the experimental data than our value. To our knowledge, no other simulation methods used to model QCLs (see Refs. [1, 23, 24] for recent reviews) have been investigated for this particular design.

5 Conclusion

In this paper, the technical details for simulations of quantum cascade lasers in real space with a non-uniform mesh and non-equilibrium Green's function method are presented. With this approach, accurate mapping of the structure of the simulated device onto its numerical model is preserved. The results of the simulations thus fit the experimental data much better than those that use constant grid sampling. In addition, this method allows the size of the numerical task to be reduced, enabling the achievement of satisfactory results much more quickly.

References

1. Jirauschek, C., Kubis, T.: Modeling techniques for quantum cascade lasers. Appl. Phys. Rev. **1**, 011307 (2014)
2. Lee, S.-C., Wacker, A.: Nonequilibrium Green's function theory for transport and gain properties of quantum cascade structures. Phys. Rev. B **66**, 245314 (2002)
3. Terazzi, R., Faist, J.: A density matrix model of transport and radiation in quantum cascade lasers. New J. Phys. **12**, 033045 (2010)
4. Kubis, T., Yeh, C., Vogl, P., Benz, A., Fasching, G., Deutsch, C.: Theory of nonequilibrium quantum transport and energy dissipation in terahertz quantum cascade lasers. Phys. Rev. B. **79**, 195323 (2009)
5. Hałdaś, G., Kolek, A., Tralle, I.: Modeling of mid-infrared quantum cascade laser by means of nonequilibrium Green's functions. IEEE J. Quantum Electron. **47**(78), 878–885 (2011)
6. Franckie, M., Winge, D.O., Wolf, J., Liverini, V., Dupont, E., Trinite, V., Faist, J., Wacker, A.: Impact of interface roughness distributions on the operation of quantum cascade lasers. Opt. Express **23**, 5201 (2015)
7. Wacker, A.: Gain in quantum cascade lasers and superlattices: a quantum transport theory. Phys. Rev. B **66**, 085326-1-7 (2002)
8. Nelander, R., Wacker, A.: Temperature dependence of the gain profile for terahertz quantum cascade lasers. Appl. Phys. Lett. **92**, 081102 (2008)
9. Wacker, A.: Coherence and spatial resolution of transport in quantum cascade lasers. Phys. Status Solid C **5**, 215 (2008)
10. Wacker, A., Nelander, R., Weber, C.: Simulation of gain in quantum cascade lasers. In: Proceedings of SPIE, 7230, 72301A-1-10 (2009)
11. Wacker, A., Lindskog, M., Winge, D.O.: Nonequilibrium Green's function model for simulation of quantum cascade laser devices under operating conditions. IEEE J. Sel. Top. Quantum Electron. **19**, 1200611-1-11 (2013)

12. Liu, Y., Lundstrom, M.: Simulation of III-V HEMTs for high-speed low-power logic applications. ECS Trans. **19**(5), 331–342 (2009)

13. Razavipour, S.G., Dupont, E., Fathololoumi, S., Chan, C.W.I., Lindskog, M., Wasilewski, Z.R., Aers, G., Laframboise, S.R., Wacker, A., Hu, Q., Ban, D., Liu, H.C.: An indirectly pumped terahertz quantum cascade laser with low injection coupling strength operating above 150 K. J. Appl. Phys. **113**(20), 1–14 (2013)

14. Yamanishi, M., Fujita, K., Edamura, T., Kan, H.: Indirect pump scheme for quantum cascade lasers: dynamics of electron-transport and very high T0-values. Opt. Express **16**(25), 20748–20758 (2008)

15. Faist, J.: Quantum Cascade Lasers. Oxford University Press, Oxford (2013)

16. Tan, I.-H., Snider, G.L., Chang, L.D., Hu, E.L.: A self-consistent solution of Schrödinger–Poisson equations using a nonuniform mesh. J. Appl. Phys. **68**, 4071–4076 (1990)

17. Svizhenko, A., Anantram, M.P., Govindan, T.R., Biegel, B., Venugopal, R.: Two-dimensional quantum mechanical modeling of nanotransistors. J. Appl. Phys. **91**(4), 2343–2354 (2002)

18. Lake, R., Klimeck, G., Bowen, R.C., Jovanovic, D.: Single and multiband modeling of quantum electron transport through layered semiconductor devices. J. Appl. Phys. **81**(12), 7845–7869 (1997)

19. Datta, S.: Electronic Transport in Mesoscopic Systems. Cambridge University Press, Cambridge (1995)

20. Kolek, A., Hałdaś, G., Bugajski, M.: Nonthermal carrier distributions in the subbands of 2-phonon resonance mid-infrared quantum cascade laser. Appl. Phys. Lett. **101**, 061110 (2012)

21. Kolek, A.: Nonequilibrium Green's function formulation of intersubband absorption for nonparabolic single-band effective mass Hamiltonian. Appl. Phys. Lett. **106**, 181102-1-5 (2015)

22. Dhar, R.S., Razavipour, S.G., Dupont, E., Xu, C., Laframboise, S., Wasilewski, Z., Hu, Q., Ban, D., Dayan, : Direct nanoscale imaging of evolving electric field domains in quantum structures. Sci. Rep. **4**, 7183 (2014)

23. Pan, A., Burnett, B., Chui, C., Williams, B.: Density matrix modeling of quantum cascade lasers without an artificially localized basis: a generalized scattering approach. Phys. Rev. B. **96**, 085308 (2017)

24. Jirauschek, C.: Density matrix Monte Carlo modeling of quantum cascade lasers. J. Appl. Phys. **122**, 133105 (2017)